Article

Shear-Induced Ordering of Nanopores and Instabilities in Concentrated Surfactant Mesh Phases

Pradip K. Bera,[§] Vikram Rathee,[§] Rema Krishnaswamy, and A. K. Sood*

Cite This: *Langmuir* 2021, 37, 6874–6886

Read Online

ACCESS | Metrics & More | Article Recommendations | Supporting Information

ABSTRACT: Mixed surfactant systems with strongly bound counterions show many interesting phases such as the random mesh phase consisting of a disordered array of defects (water-filled nanopores in the bilayers). The present study addresses the non-equilibrium phase transition of the random mesh phase under shear to an ordered mesh phase with a high degree of coherence between nanopores in three dimensions. In situ small-angle synchrotron X-ray study under different shear stress conditions shows sharp Bragg peaks in the X-ray diffraction, successfully indexed to the rhombohedral lattice with $R\bar{3}m$ space group symmetry. The ordered mesh phase shows isomorphic twinning and buckling at higher shear stress. Our experimental studies bring out rich non-equilibrium phase transitions in concentrated cationic surfactant systems with strongly bound counterions hitherto not well explored and provide motivation for a quantitative understanding.
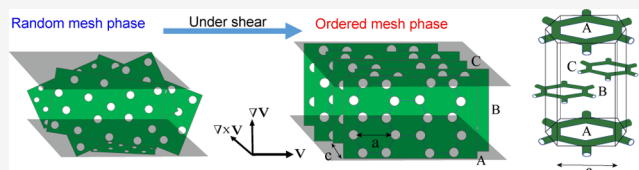
INTRODUCTION

Mesh phases are liquid crystalline phases formed in ionic as well as non-ionic mixed surfactant systems, consisting of a 1D stack of bilayers with water-filled pores or curvature defects. Depending on the correlation of these pores, the phase can be distinguished as a random mesh phase (L_α^D) if the pores exhibit a liquid-like ordering or an ordered mesh phase if the pores are correlated across the bilayers by getting locked into a three-dimensional (3D) lattice. These can be further classified as tetragonal or rhombohedral ($R\bar{3}m$) mesh phases, depending on the structural symmetry.[1−3] As a simple manifestation, the mesh phase occurring at higher surfactant concentrations is structurally similar to the adjacent lamellar phase and topologically similar to the preceding hexagonal phase formed at lower surfactant concentrations. However, non-uniform mean curvature in the mesh phase is in sharp contrast with the hexagonal or lamellar phase.[4,5] Extensive studies on the equilibrium phase behavior of lyotropic surfactant systems have established that the spontaneous formation of the defects (pores) in the mesh phase and their long-range ordering across the stack of the bilayers require a balancing of the head group interactions and the chain flexibility, particularly through the addition of a third component to a binary surfactant−water mixture.[2,6−13] Similarly, the perforated bilayers in lipid−water systems form intermediate phases due to the incorporation of proteins into the pores.[14] Random mesh phases and ordered mesh phases of different symmetries have been observed in different lyotropic mixed surfactant systems, and their equilibrium phase behavior has been well studied both theoretically and experimentally.[15] Interestingly, mesh phases are also observed in lipid−water systems and are relevant in the context of membrane fusion[16] and cytolysis.[17] Thus, a majority of the existing literature studies on mesh phases pertain to characterizing the structure of mesh phases in different ternary surfactant−water systems where these phases can be stabilized typically over a large range of surfactant concentrations.

When subjected to shear, the pore-free lyotropic lamellar phase usually exhibits two kinds of non-equilibrium phase transitions (NEPTs); one is rolling of lamellar into sphere-like structures known as multilamellar vesicles (MLVs) or onions, and the other is the change in the orientation of the bilayers. Lamellar to MLV transition was reported for the first time by Diat et al.[18] and ever since has been reported in many surfactant and polymeric systems and appears to be a common feature of the lamellar phase.[19−22] The proposed mechanism for this transition is dilation strain in the bilayers under shear which can arise due to either suppression of undulations or dislocations in the plane of the bilayers.[23] Another transition, namely, the change in the orientation, occurs in a system where the dislocation in the bilayers cannot follow shear flow and above the critical shear rate, the dilation around the dislocation destabilizes the orientation from the c-oriented state where the bilayer normal is in the gradient direction to the a-oriented state where the bilayer normal is in the vorticity direction.[20] Also, the suppression of undulations in the bilayers can result
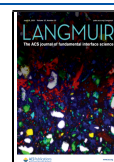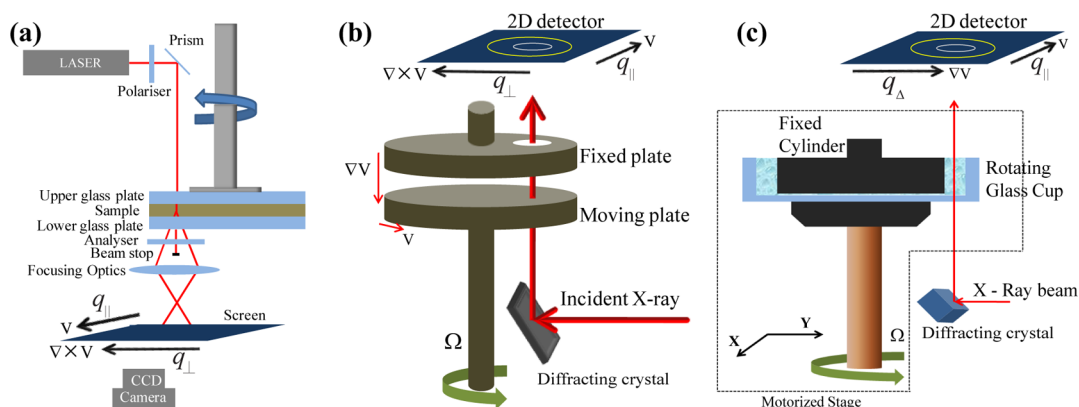
Figure 1. Schematic of the rheo-SALS setup with the PP glass geometry (a). Schematics of the rheo-SAXS setups with the PP vespel geometry (b) and with the Couette glass geometry (c). The rheo-SAXS setup with the Couette glass geometry was on a motorized stage to do the X-ray scan across the gap by varying the distance (g_x) of the X-ray from the inner static cylinder. Scattering wave vectors and different flow directions of the geometry are indicated.

in expulsion of the solvent from the bilayers.[24] According to proposed models, non-equilibrium transitions in the lamellar have been attributed to the suppression of thermal undulations causing hydrodynamical instabilities that occur above a critical shear rate which is inversely proportional to the cube of bilayer spacing and expected to occur in dilute liquid bilayer phases.[24,25] However, lamellar to onion transition is observed in concentrated bilayer forming phases well below the critical shear rate predicted by proposed theoretical models. Albeit numerous attempts, the controlled parameter for shear-induced lamellar to MLV transition remains unclear and most of these studies have been limited to bilayer systems which are stabilized by steric interactions and possess either edge or screw dislocation.

Although the kinetics of equilibrium phase transition from the mesh phase to the lamellar phase and the role of temperature as well as counterions is well understood,[1,26−30] NEPT in mesh phases formed in concentrated mixed surfactant systems remains poorly studied despite the structural similarity between the unperforated lamellar phase and the mesh phase. In comparison, in concentrated mixed surfactant systems, above the Krafft temperature, the shear-induced reversible transition from pore-free bilayers to a crystalline phase is observed at intermediate shear rates originating due to the redistribution of the counterions.[31] Similarly, shear-induced unbinding of counterions is observed in other bilayer forming or MLV phases.[32] Also, an increase in the alignment of the randomly oriented crystallites of bilayers or cylinders over macroscopic dimensions in the plane of shear as well as a transition from the random mesh phase to the onion phase has been observed under shear.[20,33] Notably, the transition to the onion phase is preceded by a change in orientation of the bilayers.

Here, we bring out a few unexplored aspects of the flow behavior of the mesh phases formed in the cationic surfactant system with strongly bound counterions. Time-resolved rheo-small-angle X-ray scattering (rheo-SAXS) measurements allow us to follow the temporal evolution of the X-ray diffraction peaks corresponding to different lattice planes of the pores of the bilayers. A reorientation of the bilayers of the L_α^D phase is always observed under shear with the bilayers stacked parallel to the shear plane (V−∇V plane) which is identified as the a-orientation. Intriguingly, further shearing reveals two distinct structural transitions depending on the separation between

bilayers of the L_α^D phase. At lower surfactant concentrations (larger bilayer separation), the a-oriented bilayers of the L_α^D phase transform to an onion phase under shear, whereas at higher surfactant concentrations (smaller bilayer separation), an NEPT from the L_α^D phase to the $R\bar{3}m$ phase is observed. The NEPT from the L_α^D phase to the $R\bar{3}m$ phase occurs through the onset of correlation of the nanopores across the bilayers before they get locked into a 3D rhombohedral lattice. This is followed by the shear-induced isomorphic twinning and buckling transition of the ordered mesh phase ($R\bar{3}m$) due to the hydrodynamic instability.

■ EXPERIMENTAL DETAILS

Materials. Surfactants cetyltrimethylammonium bromide (CTAB) and cetylpyridinium chloride (CPC) from Sigma-Aldrich were used without further purification. Sodium-3-hydroxy-2-naphthoate (SHN) was prepared by adding an equivalent amount of an aqueous solution of sodium hydroxide (NaOH) to an ethanol solution of 3-hydroxy-2-naphthoic acid (HNA). Ternary solutions of surfactant−SHN−water were prepared with deionized water (resistivity ∼18.2 MΩ·cm) for the total weight fraction of surfactant + SHN (ϕ = (Surfactant + SHN)/(Surfactant + SHN + H$_2$O)) at the desired molar ratio of the two components (α = [SHN]/[Surfactant]).[2] In equilibrium, the counterion SHN is known to be adsorbed at the micelle−water interface,[2,3,8] thus decreasing the spontaneous curvature of the micellar aggregates formed by CTAB or CPC, transforming the cylindrical micelles to pore-free bilayers as α approaches 1. The equilibrium phase diagrams of these systems (see section A in the Supporting Information) have shown random and ordered mesh phases over a wide range of surfactant concentrations (0.2 < ϕ < 0.7). In our present experiments, α was fixed at 1 for the CTAB−SHN−water system and 0.5 for the CPC−SHN−water system. The samples were well sealed and left in an oven at 40 °C for 2 weeks to equilibrate.[3] As a guide, the samples appear inhomogeneous immediately after mixing and finally become homogeneous and brownish once equilibrated with no apparent inhomogeneities seen by the naked eyes. All the measurements were done with the freshly loaded sample.

Rheo-Small-Angle Light Scattering Experiments. In situ depolarized small-angle light scattering (SALS) measurements were performed along with rheology in a shear stress-controlled rheometer (MCR 102, Anton Paar) fitted with a temperature controller (Figure 1a). A parallel plate (PP) glass geometry of a diameter of 43 mm was used with a 1 mm sample thickness. The laser beam (a wavelength of 658 nm) was in the velocity gradient direction at a fixed position of 15 mm from the plate center. SALS images on the white screen were recorded using an 8-bit color CCD camera (Lumenera, 0.75C, 1200 ×
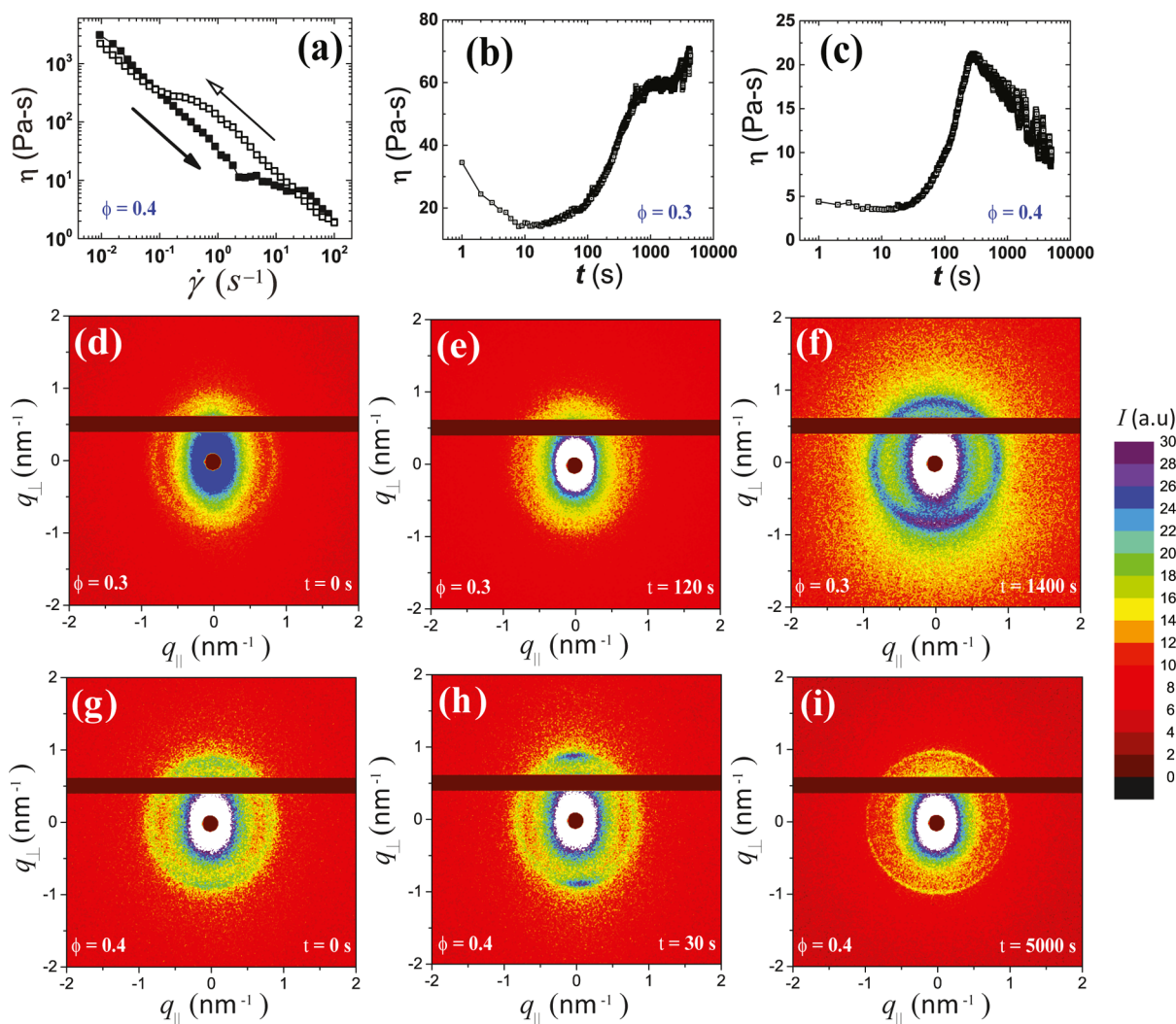
Figure 2. Shear rate-controlled measurements of the random mesh phase (L_α^D) formed in the CTAB−SHN−water system $(\alpha = 1)$ done in the PP geometry. (a) Flow curve for $\phi = 0.40$; viscosity vs shear rate $(\eta$ vs $\dot\gamma)$ with a 30 s waiting time at each data point. The filled symbol and empty symbol represent increasing and decreasing $\dot\gamma$, respectively, as indicated by arrows. (b) Shear stress relaxation for $\phi = 0.30$; viscosity vs time $(\eta$ vs $t)$ at $\dot\gamma = 10$ s^{-1} and the observed X-ray diffraction pattern at $t = 0$ s (d), $t = 120$ s (e), and $t = 1400$ s (f). (c) Similar shear stress relaxation for $\phi = 0.40$; η vs t at $\dot\gamma = 10$ s^{-1} and the observed X-ray diffraction pattern at $t = 0$ s (g), $t = 30$ s (h), and $t = 5000$ s (i). The intensity color scale (shown in the rightmost) is the same for all the patterns in this figure.

980 pixels) fitted with a PENTAX TV Lens of a focal length of 12 mm.

Rheo-SAXS Experiments. We have used a time-resolved SAXS setup coupled with a Haake−Mars rheometer[34] at the P10 beamline of the PETRA III synchrotron (Figure 1b,c). The sample chamber was fitted with a Peltier-based temperature controller and a humidity controller with a slow nitrogen flow. The synchrotron X-ray beam was deflected vertically and passed through the sample. The X-ray diffraction patterns were recorded on a Pilatus 300 K detector with a varying exposure time of 10−50 s. For the PP Vespel geometry (DuPont, diameter 35 mm), the sample thickness was chosen to be 1 mm due to the high absorbance, and the X-ray beam was in the velocity gradient direction at a fixed position of 13 mm from the plate center. The detector was placed parallel to the vorticity plane (**V**−∇×**V** plane) at a distance of 1000 mm from the sample. For the Couette glass geometry (with a metallic inner cylinder of a diameter of 29 mm and an outer glass cup of a diameter of 33 mm), the sample height was 5.5 mm, and the X-ray beam was parallel to the vorticity direction with the detector plane parallel to the shear plane (**V**−∇**V** plane). The position of the beam was varied in Couette's radial direction by slowly translating the motorized stage of the rheometer.

■ RESULTS AND DISCUSSION

Otherwise stated, here, all the measurements were done at 30 °C (above the Krafft temperature of 25 °C) with the PP Vespel geometry having a sample thickness of 1 mm. Following the model in ref 7, we have estimated the size of the water-filled pores ($\sim\sqrt[3]{\text{pore volume}}$) to be in the range from 3.7 to 4.6 nm (see section B in the Supporting Information), hence justifying calling the pores as nanopores.

Non-equilibrium Phase Transition from the Random Mesh Phase (L_α^D) to the Onion Phase. We start with the CTAB−SHN−water system for $\phi < 0.5$ and $\alpha = 1$ for which the flow curve is shown in Figure 2a, recorded with the waiting time at each shear stress to be 30 s. We point out that these flow curves are not steady-state flow curves as the system evolves with time under the application of shear stress. It can be seen that the random mesh phase (L_α^D) exhibits a typical shear-thinning behavior where the viscosity (η) decreases with the shear rate or with the shear stress. At smaller shear rates, the lamellae sheets flow and pass each other, resulting in a
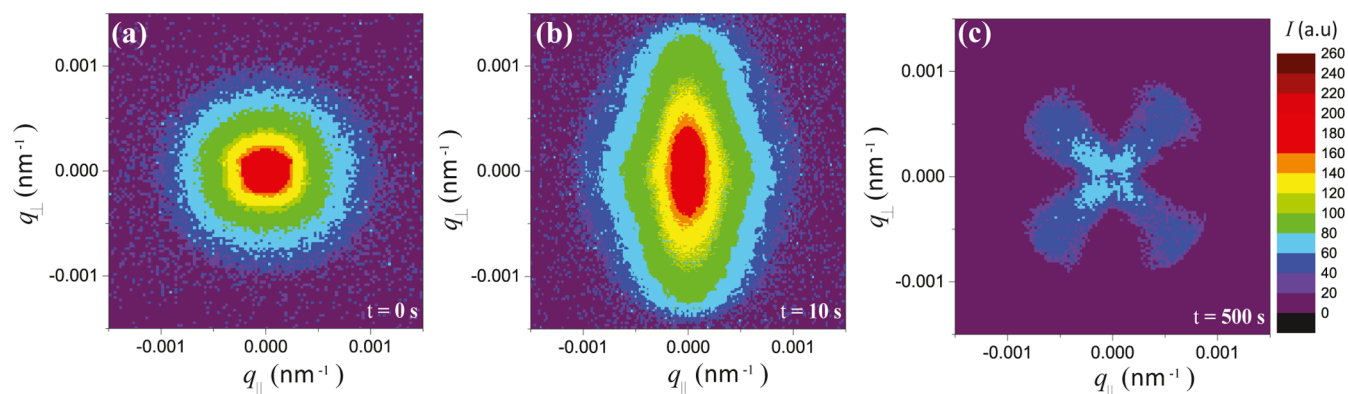
Figure 3. During the shear stress relaxation of L_α^D similar to Figure 2c, SALS patterns observed at $t = 0$ (a), $t = 10$ (b), and $t = 500$ s (c) are shown ($\phi = 0.40$, $\alpha = 1$, $\dot{\gamma} = 10$ s^{-1}). The intensity color scale (shown in the rightmost) is the same for all the patterns in this figure.

sharp decrease in η before showing an inflection point, followed by another shear-thinning region. In the reverse run, we observe only shear-thinning behavior, suggesting that the observed structural changes are not shear-reversible. Since flow curve measurements are time-averaged over several seconds at a particular shear rate, time-resolved rheology reveals temporal evolution of viscosity at a constant shear rate. Figure 2b,c shows the evolution of η at a constant shear rate ($\dot{\gamma}$) of 10 s^{-1} for two different volume fractions $\phi = 0.3$ and 0.4, respectively, at $\alpha = 1$. For both values of ϕ, η shows a minimum at $t \sim 10$ s and then increases to a high value. For $\phi = 0.3$, without shear, the X-ray diffraction pattern shows an isotropic Bragg ring having a very weak intensity due to the randomly oriented domains of lamellae having d-spacing $d_l = 9.60$ nm (Figure 2d). Here, we do not observe the diffuse scattering peak due to the lack of in-plane correlation between nanopores. Before $t = 1000$ s, the intensity of the isotropic Bragg ring becomes even lesser (Figure 2e), indicating a partially oriented lamellar phase with predominantly c-oriented bilayers. This is further evident from the low viscosity of the sheared sample at around 120 s compared to the starting phase as the c-orientation of the bilayers (the schematic is shown in Figure 10B) offers a lower resistance to shear. However, in the steady state after $t = 1000$ s, a sharp isotropic Bragg ring is observed, suggesting the formation of the onion phase under shear (Figure 2f). For $\phi = 0.4$, without shear, the observed unoriented lamellae (Figure 2g) have a d-spacing of $d_l = 7.05$ nm and the nanopores have an in-plane correlation length of $d_d = 7.68$ nm (Supporting Information, Table S1). For $t \geq 10$ s, a-orientation of the bilayers[35] is observed (the schematic is shown in Figure 10A) where the lamellar peak (the Bragg peak due to the lamellar periodicity) is sharp in the vorticity direction (in the $\nabla \times \mathbf{V}$ direction or $\mathbf{q}_\perp$ direction) and the diffuse scattering peak becomes sharp in the flow direction (in the $\mathbf{V}$ direction or $\mathbf{q}_\parallel$ direction), indicating bilayer planes stacked parallel to the $\mathbf{V} - \nabla \mathbf{V}$ plane (called the shear plane) (Figure 2h). Here, we note that for $\phi = 0.4$, the shear alignment of the L_α^D phase was useful to distinguish the lamellar peak and the diffuse peak clearly as they are almost overlapping in the equilibrium diffraction pattern. The observed decrease in viscosity corresponding to the a-orientation indicates that the bilayers offer less resistance to shear in this configuration. After $t = 1000$ s, a sharp isotropic Bragg ring is observed, suggesting the formation of the onion phase under shear (Figure 2i). The observed induction time of about 10 to 20 s in both the systems beyond which the viscosity increases is likely to be

associated with the time to align a certain portion of the multidomain L_α^D phase. The order of induction time is similar to that in the other study[36] where they show that the induction time decreases with increasing shear rate. The Fourier transform of the fluctuations in η (Figure 2b,c) gives a time scale of ~12 s (the plots are not shown), which is very close to the time period of one rotation of the plate confining the sample. In order to assign any meaning to these oscillations, much more studies in future are required to ascertain shear banding-induced instabilities without the artifact of slip at the sample−plate interface.

Further, we have used the in situ SALS to confirm the NEPT from the L_α^D phase to the onion phase by observing a four-lobed clover-leaf pattern, a signature of the onion under the depolarized SALS.[20] The rheo-SALS measurements were performed in the VH (polarizer ⊥ analyzer) configuration. Figure 3 shows the evolution of rheo-SALS patterns obtained during the shear stress relaxation measurement of the L_α^D phase for $\phi = 0.4$ at $\dot{\gamma} = 10$ s^{-1}. The time evolution of η is the same as that in Figure 2c (data not shown). At $t \sim 10$ s, the isotropic pattern (Figure 3a) changes to an anisotropic pattern (Figure 3b), oriented parallel to the $\mathbf{q}_\perp$ direction indicating the flow alignment of bilayers parallel to the shear plane. After $t = 500$ s, the expected four-lobed clover-leaf pattern associated with the onion phase appears (Figure 3c). The observed clover-leaf pattern in SALS arises from the optical anisotropy of the onions where two refractive indices that are parallel and perpendicular to the radial direction can be defined and very similar to that obtained from spherulites of semi-crystalline polymers.[37] When the onion phase with the optic axis along the radial direction (normal to the bilayers) is placed between crossed polarizers, a four-lobed pattern is obtained in SALS where maximum intensity is observed at 45° and minimum at 0°, 90°. The increase in η is due to the NEPT from well-separated lamellae to closely packed onions. After 1000 s, the observed fluctuations in the η are possibly due to the onions' rearrangements or variation in the size of these onions.[38] Although the NEPT from the L_α^D phase to the onion phase under shear is a well-studied phenomenon,[20] the noteworthy aspect of the present study is that lamellar to onion transition is not limited to dilute lamellar phase or bilayers having defects in the form of dislocations but also observed in bilayers having defects in the form of solvent-filled pores. In our study, we find that L_α^D to onion transition occurs for a bilayer separation greater than 7 nm. Before transition to the onion phase, the orientation of bilayers strongly depends on the pore spacing. In
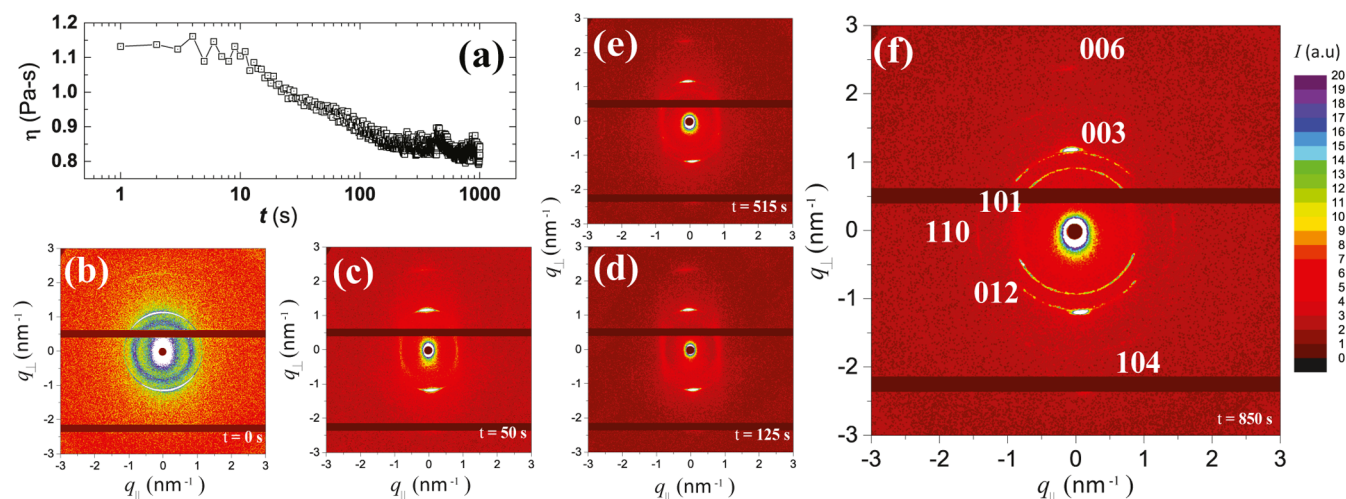
Figure 4. Shear stress relaxation of L_α^D for $\phi = 0.50$ (CTAB−SHN−water; $\alpha = 1$) at $\dot{\gamma} = 50$ s^{-1} done in the PP geometry. (a) η vs t and the observed X-ray diffraction patterns at $t = 0$ s (b), $t = 50$ s (c), $t = 125$ s (d), $t = 515$ s (e), and $t = 850$ s (f) are shown. $R\bar{3}m$ lattice planes are marked near the observed Bragg rings in (f). The intensity color scale (shown in the rightmost) is the same for all the patterns in this figure.

particular, we have observed a-orientation at $\phi = 0.3$ and c-orientation at $\phi = 0.4$. A schematic of this transition is shown in Figure 10C.

Shear-Induced 3D Ordering of Nanopores in the L_α^D Phase. The concentrated L_α^D phase formed in the CTAB−SHN−water system at $\phi = 0.5$ and $\alpha = 1$ demonstrates an NEPT from the L_α^D phase to the $R\bar{3}m$ phase under shear. On applying a constant shear rate of $\dot{\gamma} = 50$ s^{-1}, η of the L_α^D phase decreases with time and it reaches the steady state after $t \sim 200$ s (Figure 4a). Figure 4b−f shows the temporal evolution of the X-ray diffraction pattern. In the quiescent state, the X-ray diffraction pattern (Figure 4b) reveals two isotropic Bragg rings with their q ratio of 1:2 (characteristic of an unaligned lamellar phase), with $d_l = 5.49$ nm (Supporting Information, Table S1). As expected in a random mesh phase, the diffuse isotropic ring observed at a smaller angle confirms the existence of liquid-like correlated nanopores (water-filled) in the plane of the bilayer with an average in-plane correlation length of $d_d = 7.67$ nm. The nearly isotropic rings corresponding to the lamellar periodicity of bilayers and the liquid-like correlation of the in-plane nanopores evolve to the well-aligned anisotropic diffraction pattern at $t \sim 50$ s, revealing the a-oriented state of the bilayers (Figure 4c). The occurrence of the diffuse scattering peaks as arcs azimuthally centered at $\mathbf{q}_\parallel \sim 0$ suggests an absence of the *trans*-bilayer correlation of the nanopores. Notably, at $t \sim 515$ s, the azimuthal intensity profile of the diffuse scattering peak shows a splitting away from $\mathbf{q}_\parallel = 0$ (Figure 4e), suggesting the onset of long-range correlation of the nanopores across the bilayers favoring the formation of a 3D ordered structure. At $t \sim 850$ s (Figure 4f), a few more peaks appear in the X-ray diffraction pattern, with no further change upon shearing up to 1000 s, indicating a steady state. The temporal evolution of the SAXS diffractogram during this transition is presented in section C in the Supporting Information (Figure S3). All the partially oriented Bragg reflections of the diffraction pattern shown in Figure 4f could be indexed to a rhombohedral lattice with the $R\bar{3}m$ space group with lattice parameters $a = 8.68$ and $c = 15.93$ nm, coexisting with the L_α^D phase (Supporting Information, Table S3). The lamellar reflection of the L_α^D phase overlaps with the (003) reflection of the $R\bar{3}m$ phase (lamellar

periodicity $\sim c/3 = 5.31$ nm), and its coexistence with the $R\bar{3}m$ phase in the final steady state is inferred from the diffuse arcs azimuthally centered at $\mathbf{q}_\parallel \sim 0$. With both the phases in the steady state, the shear-banding situation is possible where both the phases experience different shear rates.

We have chosen the following $R\bar{3}m$-indexing scheme where the first reflection overlapping with the diffuse scattering peak from the nanopores is indexed as (101) and the third reflection which lies on the $\mathbf{q}_\perp$ axis as the (003) reflection. As seen from Table S3 in the Supporting Information, the second reflection appearing as the shoulder of the (003) reflection is indexed as the (012) reflection. Moreover, the (110) reflection corresponding to scattering from the in-plane nanopores of the bilayers lies parallel to $\mathbf{q}_\parallel$, further confirming the robustness of our indexation to the diffraction peaks of the $R\bar{3}m$ structure. The structure of the shear-induced $R\bar{3}m$ phase could be modeled as an ordered mesh phase with ABC stacking of three-connected rods.[8] Moreover, the lattice parameters obtained for the shear-induced $R\bar{3}m$ phase are similar to those obtained for the equilibrium $R\bar{3}m$ phase at $\phi = 0.53$. Using the lattice parameters (a, c) and the above discussed three-connected rod model, the estimated value of the micellar radius (r_m) is 2.10 nm, consistent with the equilibrium value reported in ref 8. We propose that during this NEPT, the decrease in viscosity η is due to the persistence of a-orientation of the bilayers that offers low resistance to shear as well as due to the 3D ordering of the nanopores (the schematic is shown in Figure 10D) that provides the passage for the liquid to pass through the connected pores. To quantify the reversibility of the L_α^D to $R\bar{3}m$ transition, we stopped the shear after 1000 s and follow the SAXS diffraction pattern with time. Since the (003) reflection corresponds to both the L_α^D and $R\bar{3}m$ phases, we follow (101) and (110) Bragg peaks of the shear-induced $R\bar{3}m$ whose intensities decrease with time (see section C in the Supporting Information, Figure S4), confirming reversibility of the transition.

To ascertain that the NEPT from the L_α^D phase to the $R\bar{3}m$ phase is generic, at least to other cationic surfactant systems with strongly bound counterions, we have also studied the concentrated L_α^D phase (with $d_l = 5.13$ nm and $d_d = 6.50$ nm) formed in the CPC−SHN−water system ($\phi = 0.55$ and $\alpha = $
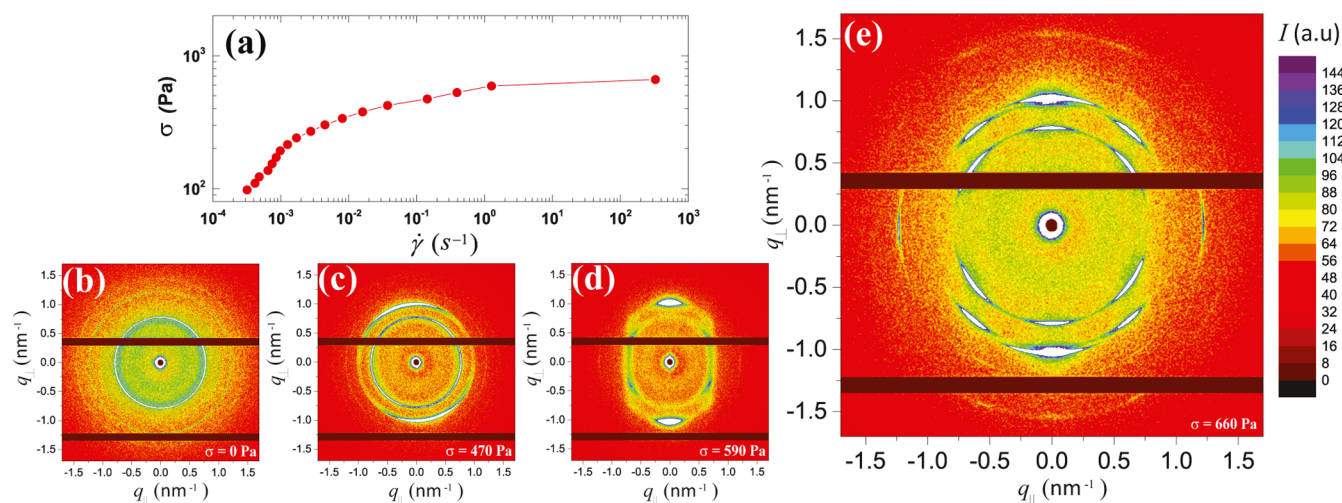
Figure 5. Shear stress-controlled flow curve of the rhombohedral mesh phase ($R\bar{3}m$) formed in the CTAB−SHN−water system ($\alpha = 1$, $\phi = 0.53$) done in the PP geometry. (a) Shear stress vs shear rate (σ vs $\dot{\gamma}$) plot with a 200 s waiting time at each data point. Observed X-ray diffraction patterns for $\sigma = 0$ Pa (b), $\sigma = 470$ Pa (c), $\sigma = 590$ Pa (d), and $\sigma = 660$ Pa (e) are shown. The intensity color scale (shown in the rightmost) is the same for all the patterns in this figure.

$0.5)^3$. In this case also, we have observed a similar NEPT from the L_α^D phase to the $R\bar{3}m$ phase (see section D in the Supporting Information). The viscosity η decreases with time but reaches the steady state after $t \sim 20$ s (section D in the Supporting Information, Figure S5a) in a comparatively short period of time (compared to the CTAB−SHN−water system shown in Figure 4). Under shear, the L_α^D phase goes to the coexistence of two $R\bar{3}m$ phases with lattice parameters $a1 = 8.39$, $c1 = 14.79$ and $a2 = 8.27$, $c2 = 14.28$ nm (Supporting Information, Table S2). After stopping the shear, the temporal evolution of the SAXS diffractogram shows a complete reversibility from the shear-induced $R\bar{3}m$ phase to the L_α^D phase within 10 s (section D in the Supporting Information, Figure S6). From our observations on these two systems, we suggest that the shear-induced ordering of the water-filled nanopores is expected in systems where both the random mesh phase and the ordered mesh phase are present adjacent to each other in the equilibrium phase diagram. However, the control parameters of the transition will depend on the d-spacing, stabilizing forces, water pore size, etc.

Mechanism of the Shear-Induced $R\bar{3}m$ Ordering of the Nanopores of L_α^D. The shear-induced $R\bar{3}m$ phase obtained in two different systems on applying a constant shear rate indicates that this NEPT is a general feature of concentrated random mesh phases. The distinguishing feature governing the kinetics of the NEPT from the L_α^D phase to the $R\bar{3}m$ phase at a constant shear rate, which may be identified in both these systems from the time-resolved rheo-SAXS measurements, is the a-orientation of the lamellae prior to the appearance of the sharp (101) reflection corresponding to the 3D ordering of nanopores. In the presence of thermal undulations, the a-orientation of bilayers in the lamellar phase is usually preferred at high shear rates since the suppression of thermal undulations under shear is lower in the a-orientation in comparison with the c-oriented state (where the bilayer planes are stacked parallel to the $\mathbf{V}-\nabla\times\mathbf{V}$ plane, called the vorticity plane).[39]

We propose that the locking of the nanopores into a 3D lattice occurs when the in-plane correlation length of the nanopores (d_d) is larger than the bilayer periodicity (d_l). A

comparison can be drawn here with respect to the equilibrium phase behavior of the system (CTAB−SHN−water system, $\alpha = 1$), where the L_α^D phase to $R\bar{3}m$ phase transition is observed with decreasing water content (for $\phi > 0.5$). The in-plane periodicity ratio (Γ) is estimated from the ratio of d_d (or lattice parameter a in the case of $R\bar{3}m$) to the bilayer separation d_l for the L_α^D phase (or lattice parameter $c/3$ in the case of $R\bar{3}m$). We find that when the surfactant volume fraction ϕ increases from 0.5 to 0.53, Γ increases from a value of 1.2 in the L_α^D phase to 1.4 in the $R\bar{3}m$ phase. A crucial aspect favoring our argument would be an increase in d_d with shear observed from the diffuse scattering peak positions. However, domains of L_α^D with an increased d_d are not observed in our experiments, possibly because the strong flow imposed on the sample at a high shear rate smears out the diffraction pattern from these domains, giving rise to a broad and diffuse scattering peak. Nevertheless, it should be noted that an increase in pore size at a constant water content (ϕ) implies that water from the inter-bilayer region will enter into the nanopores, thus decreasing the bilayer separation. Hence, the observed decrease in the lamellar periodicity by ∼3 Å under shear reinforces the proposed shear-induced increase in average pore size. Further, the consequent increase in Γ from 1.3 to 1.6 for the shear-induced $R\bar{3}m$ phase is consistent with the increase in Γ observed for the L_α^D phase to $R\bar{3}m$ phase transition on decreasing water content in equilibrium.[8]

We note that the equilibrium phase behavior of the CTAB−SHN−water system[2] indicates that for higher molar ratios of SHN to CTAB ($\alpha > 1$), the $R\bar{3}m$ mesh phase can occur at a lower surfactant concentration. Here, under shear, a rearrangement of the organic salt/counterions on the bilayers can increase α locally, driving the transition to the $R\bar{3}m$ mesh phase at lower surfactant concentrations. Similar shear-induced phase transitions have been reported in cationic−anionic mixed surfactant systems[31] where transition from isotropic to crystalline as well as lamellar to crystalline phases was observed. It is noteworthy that the NEPT from the L_α^D phase to the $R\bar{3}m$ phase is absent at lower surfactant volume fractions for $\phi < 0.5$, having $\alpha = 1$. A robust conclusion that emerges from our studies on the concentrated random mesh phase is
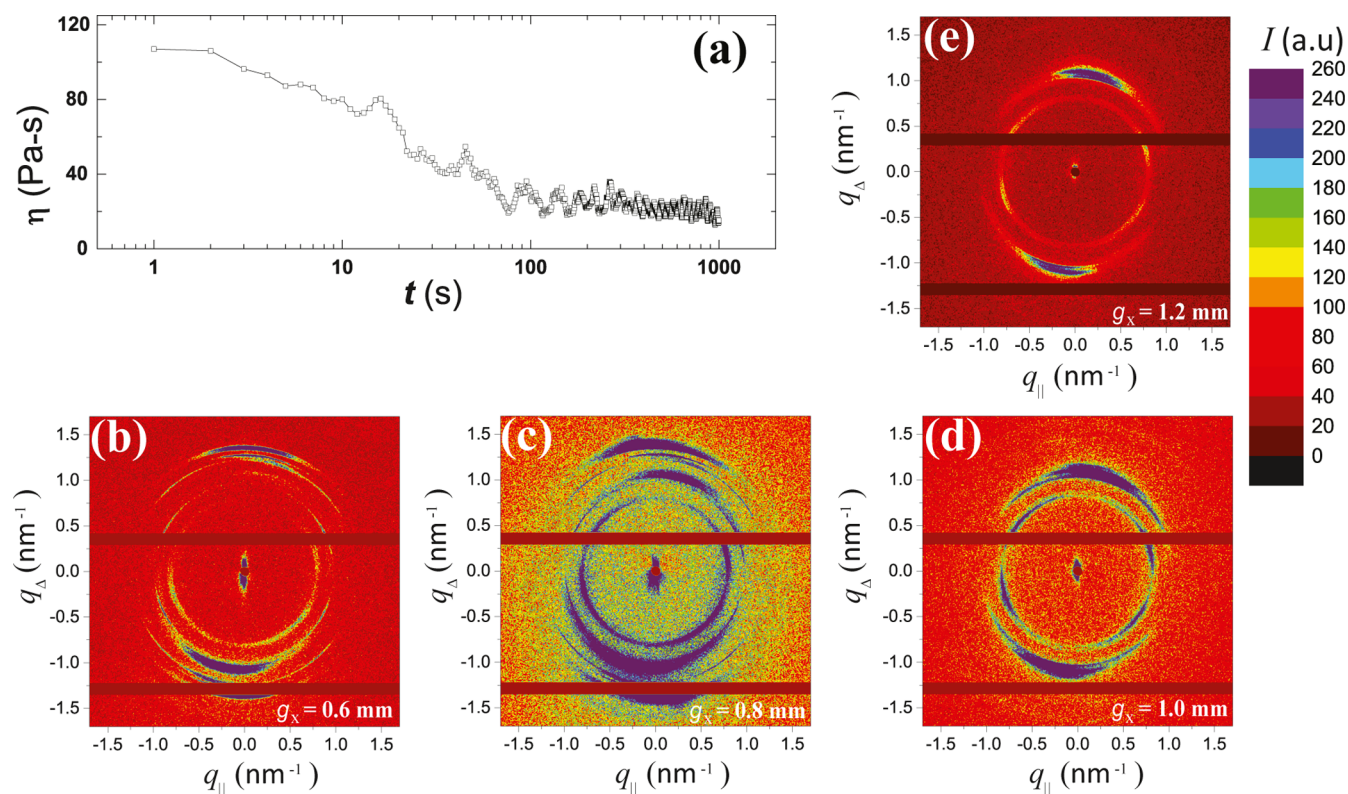
Figure 6. Shear stress relaxation of $R\bar{3}m$ (CTAB−SHN−water system, $\alpha = 1$, $\phi = 0.53$) at $\dot{\gamma} = 1$ s^{-1} done in the Couette geometry. (a) η vs t and the X-ray diffraction patterns observed during 700 s $\leq t \leq$ 850 s, with the incident X-ray beam at different distances (g_x) from the inner static cylinder; (b) $g_x = 0.6$ mm, (c) $g_x = 0.8$ mm, (d) $g_x = 1.0$ mm, and (e) $g_x = 1.2$ mm. The intensity color scale (shown in the rightmost) is the same for all the patterns in this figure.

that a shear-induced ordering of the membrane nanopores occludes the formation of onion phases.

Plastic Deformation of the $R\bar{3}m$ Phase during Flow. We will now present the effects of shear flow on the randomly oriented crystallites of the $R\bar{3}m$ phase for different values of ϕ (see section E in the Supporting Information for the SALS and SAXS measurements with the equilibrium $R\bar{3}m$ phase). Figure 5a shows the shear stress-controlled flow curve of the $R\bar{3}m$ phase (CTAB−SHN−water, $\phi = 0.53$, $\alpha = 1$) with a stepwise increment in shear stress with a 200 s waiting time at each data point. The waiting time of 200 s is not enough to reach strain of order 1, and hence, the inflection point at a strain rate of ∼0.001 s^{-1} may not correspond to a physical effect. The flow curve reported at small shear rates (below 5×10^{-3} s^{-1}) is only qualitative.

The diffraction pattern of the randomly aligned sample at σ = 0 Pa (Figure 5b) progressively transforms to the perfectly aligned sample (a-oriented state) at $\sigma = 590$ Pa with $\dot{\gamma} \sim 1$ s^{-1} (Figure 5c,d). The X-ray diffraction pattern of the perfectly aligned phase (Figure 5d) has four diffuse arcs in (101), (012) Bragg rings and has two concentrated arcs in the (003) Bragg ring, consistent with the rotational symmetry of reciprocal lattice points of $R\bar{3}m$.[16] At $\sigma = 660$ Pa (corresponding $\dot{\gamma} \sim 100$ s^{-1}), six arcs are observed in (101), (012) Bragg rings, which we propose are due to buckling[40] with two different states of orientation, that is, the presence of two directors (Figure 5e) (the schematic is shown in Figure 10E), consistent with the observed star-like pattern in the rheo-SALS measurement (see section F in the Supporting Information). In rheo-SALS, the pattern is wide in two different directions (nearly orthogonal), which can be interpreted that the system has two preferred

directions of bilayer orientations during flow. The lattice parameters of $R\bar{3}m$ remain the same before and after the buckling (Supporting Information, Table S4). For $\sigma > 700$ Pa, an extreme shear thinning is observed.

To probe this transition at different positions in the shear gradient direction in the PP geometry, the X-ray has to pass through the sample at an angle to the vorticity direction that is not feasible in the present scattering geometry. To overcome this difficulty, we have used the Couette geometry as discussed below. The X-ray beam was translated in the gradient direction to place the beam at different positions (g_x) in the Couette gap. In the PP geometry, the structural transition occurs at $\dot{\gamma} \sim 1$ s^{-1}; thus, here, we have followed the temporal evolution of the X-ray diffraction patterns during the shear stress relaxation at $\dot{\gamma} = 1$ s^{-1} (Figure 6). The viscosity shows a monotonic decay up to ∼100 s and then fluctuates about 20 Pa s in the steady state. The X-ray diffraction patterns were recorded after 700 s. Remarkably, an unexpected rich sequence of orientational transition accompanies the coexistence of two $R\bar{3}m$ phases as discussed below. The equilibrium sharp isotropic (003) Bragg ring becomes sharp in the velocity gradient direction (the ∇V direction or q_Δ direction), and the aligned diffraction pattern is called the c-oriented state, indicating that the correlated bilayer planes are stacked parallel to the vorticity plane. The X-ray diffraction patterns for four different g_x show the coexistence of two $R\bar{3}m$ phases with different lattice parameters (Supporting Information, Table S5). The relative orientation of these two $R\bar{3}m$ phases changes with g_x as the incident X-ray beam is taken from the stator toward the rotor. Our measurements with the $R\bar{3}m$ phase in both the shearing geometries suggest that both "a" and "c"-oriented bilayers coexist. However, with
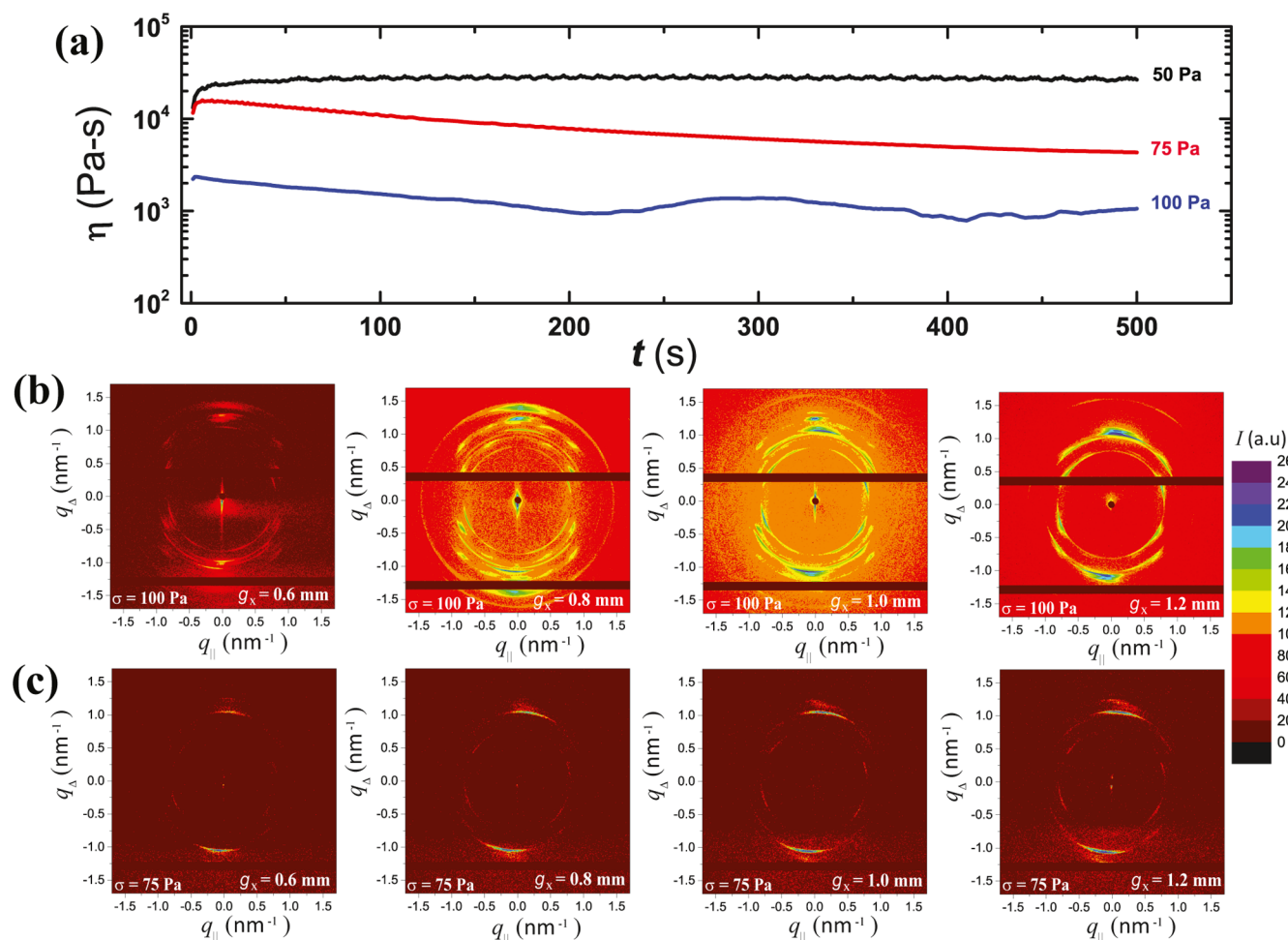
Figure 7. Shear rate relaxation of $R\bar{3}m$ (CTAB−SHN−water system, $\alpha = 1$, $\phi = 0.53$) done in the Couette geometry. (a) η vs t at different applied σ. X-ray diffraction patterns for different g_x are shown, row (b) for $\sigma = 100$ Pa and row (c) for $\sigma = 75$ Pa. For each measurement, a fresh sample was loaded and SAXS was done during $300\ \text{s} \leq t \leq 450\ \text{s}$. The intensity color scale (shown in the rightmost) is the same for all the patterns in this figure.

the shearing geometries used, we cannot probe these two orientations simultaneously. In particular, here, the a-orientation (c-orientation) will not be observed in the plate−plate (Couette cell) geometry.

We have also performed the shear rate relaxation measurements on an unaligned $R\bar{3}m$ phase in the Couette geometry (Figure 7). For $\sigma < 100$ Pa, the system flows with a partially c-oriented $R\bar{3}m$ throughout the gap between shearing cylinders (Figure 7c). On applying a high shear stress ($\sigma = 100$ Pa), the diffraction pattern shows several Bragg rings (Figure 7b). Coexistence of two $R\bar{3}m$ phases with different lattice parameters (Supporting Information, Table S6) is observed in all the diffraction patterns for all g_x, except for $g_x = 1.2$ mm (here, only the starting $R\bar{3}m$ phase is observed). The relative orientation of these two $R\bar{3}m$ changes with g_x as one goes from the stator to the rotor. The presence of six or eight arcs in (101), (012) Bragg rings near the inner static cylinder (Figure 7b) suggests buckling of $R\bar{3}m$ with two different states of the orientation of nanocrystallites with the same lattice parameters. The lattice parameters a and c of the two $R\bar{3}m$ phases do not show any significant change in the shear gradient direction (see section G in the Supporting Information), suggesting sample uniformity during shear. The isomorphic twinning of the $R\bar{3}m$ phase has substantial variation in the relative orientation of the

directors as one goes from the stator to the rotor. This suggests that the buckling angle can vary in the velocity gradient direction, and the crystallites corresponding to different directors may have different lattice parameters.

Now, we correlate the modulation in the X-ray diffraction to the domains' orientation deep inside the sample under shear (e.g., Figure 5d,e). At a moderate shear rate, the $R\bar{3}m$ phase has an a-aligned state with all layers facing toward the vorticity direction. The X-ray diffracting in a perpendicular direction to the layer normal will show two strong arcs in the (003) Bragg ring and four arcs in (012), (101) Bragg rings due to lattice symmetry of $R\bar{3}m$. At a high shear rate, few layers still retain the a-oriented state, whereas others reorient themselves at a certain angle ($\sim$45°) with the vorticity direction, giving rise to more than four arcs in (012), (101) Bragg rings. The absence of many arcs in the (003) Bragg ring can be due to the fact that the (003) diffraction has only twofold symmetry and the reoriented layers can easily miss it due to the finite angle with the shear gradient direction. This scenario is depicted in Figure 10D. Note that a similar model has been used to explain the small-angle scattering data from the Kraton-type block copolymers during tensile deformation where four arcs were observed in place of two in the Bragg ring corresponding to the spacing between cylinders.[41]
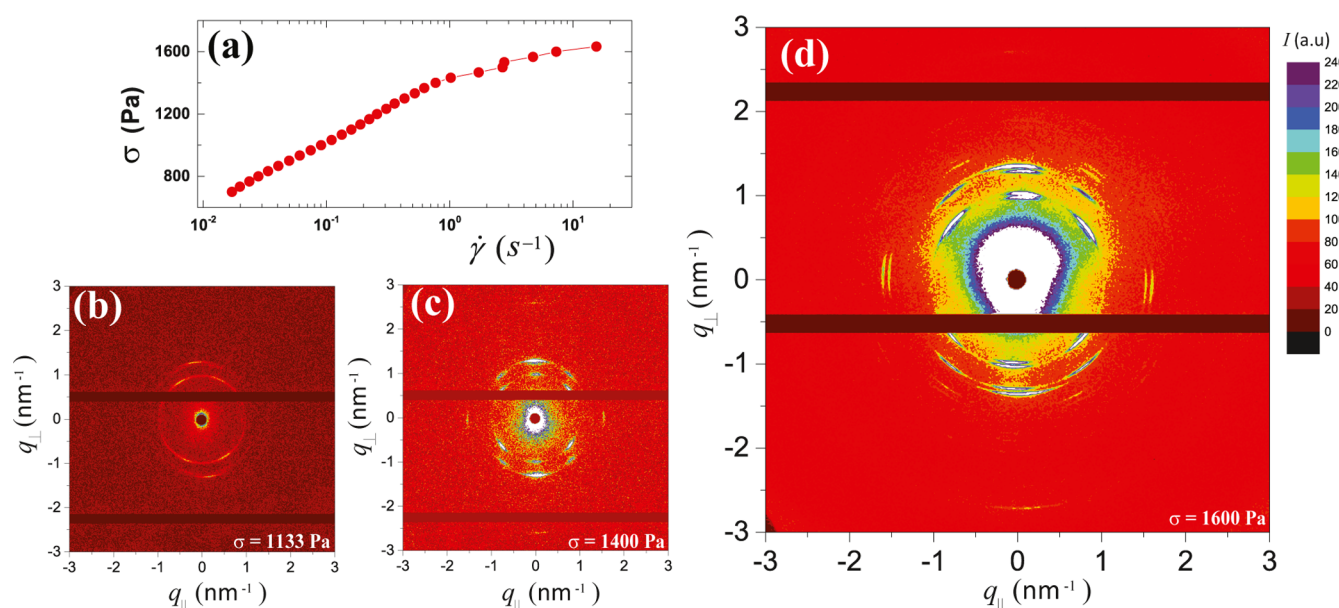
Figure 8. Shear stress-controlled flow curve of $R\overline{3}m$ (CTAB−SHN−water, $\alpha = 1$, $\phi = 0.6$) done in the PP geometry. (a) σ vs $\dot{\gamma}$ and the observed X-ray diffraction patterns for $\sigma = 1133$ Pa (b), $\sigma = 1400$ Pa (c), and $\sigma = 1600$ Pa (d) are shown. The intensity color scale (shown in the rightmost) is the same for all the patterns in this figure.
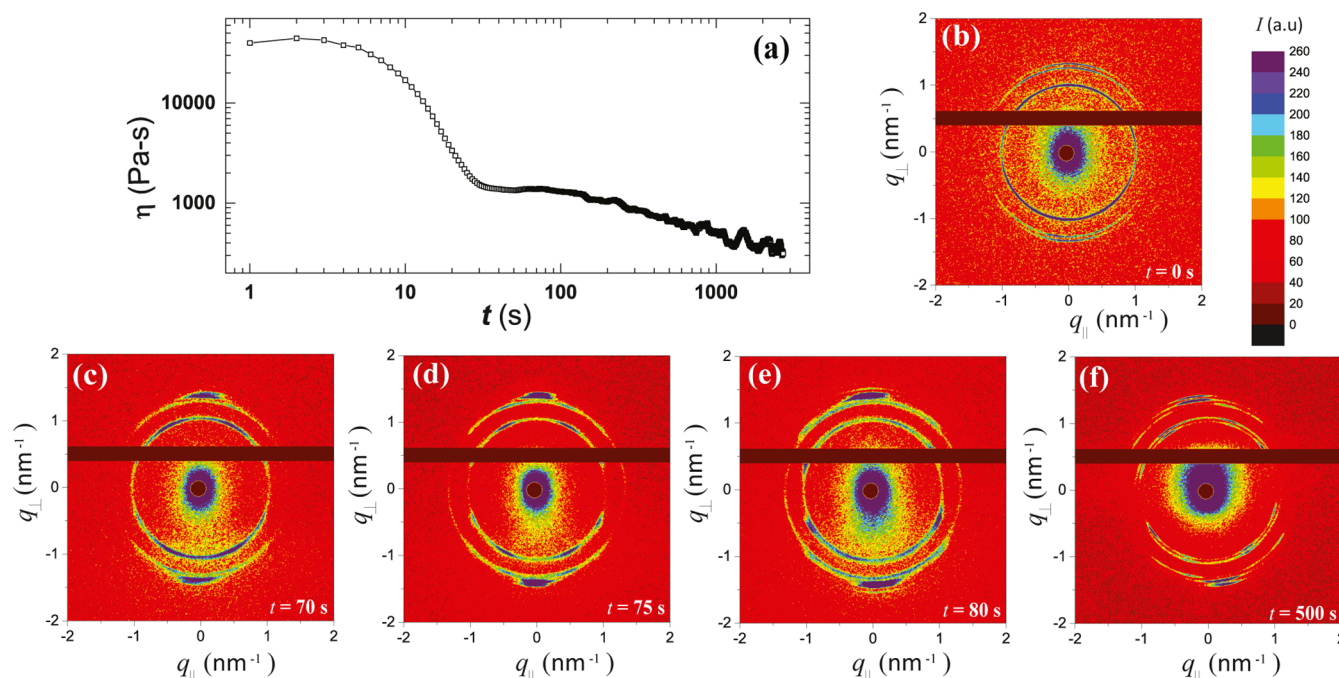

Figure 9. Shear stress relaxation of $R\overline{3}m$ (CTAB−SHN−water system, $\alpha = 1$, $\phi = 0.60$) at $\dot{\gamma} = 1$ s^{-1} done in the PP geometry. (a) η vs t and the observed X-ray diffraction patterns at $t = 0$ s (b), $t = 70$ s (c), $t = 75$ s (d), $t = 80$ s (e), and $t = 500$ s (f) are shown. The intensity color scale (shown in the right corner) is the same for all the patterns in this figure.

The concentrated $R\overline{3}m$ phase (CTAB−SHN−water, $\phi = 0.60$, $\alpha = 1$) also shows the buckling and the coexistence of two $R\overline{3}m$ phases under shear as discussed below. The shear stress-controlled flow curve is obtained by varying the shear stress in the range of 700−1700 Pa in 30 logarithmic steps with a waiting time of 50 s per data point (Figure 8a). The unaligned diffraction pattern transforms to an aligned pattern at $\sigma = 1133$ Pa (Figure 8b). Four diffuse arcs appear on the (101) Bragg ring of $R\overline{3}m$. For $\sigma = 1400$ Pa (corresponding $\dot{\gamma} \sim 1$ s^{-1}), six arcs are observed on the (101) Bragg ring as well as the

azimuthal spread of the arcs becomes smaller (Figure 8c). For $\sigma = 1600$ Pa (corresponding $\dot{\gamma} \sim 10$ s^{-1}), two $R\overline{3}m$ phases with different lattice parameters appear (Figure 8d). The two sets of lattice parameters ($a = 8.13$ nm, $c = 13.80$ nm) and ($a = 7.69$ nm, $c = 13.80$ nm) (Supporting Information, Table S7) show lower values compared to the equilibrium lattice parameters ($a = 8.30$ nm, $c = 14.10$ nm). We have followed the temporal evolution of the X-ray diffraction pattern during the shear stress relaxation measurement at 1 s^{-1} (Figure 9a). Again, the sharp isotropic Bragg rings in the quiescent state (Figure 9b)
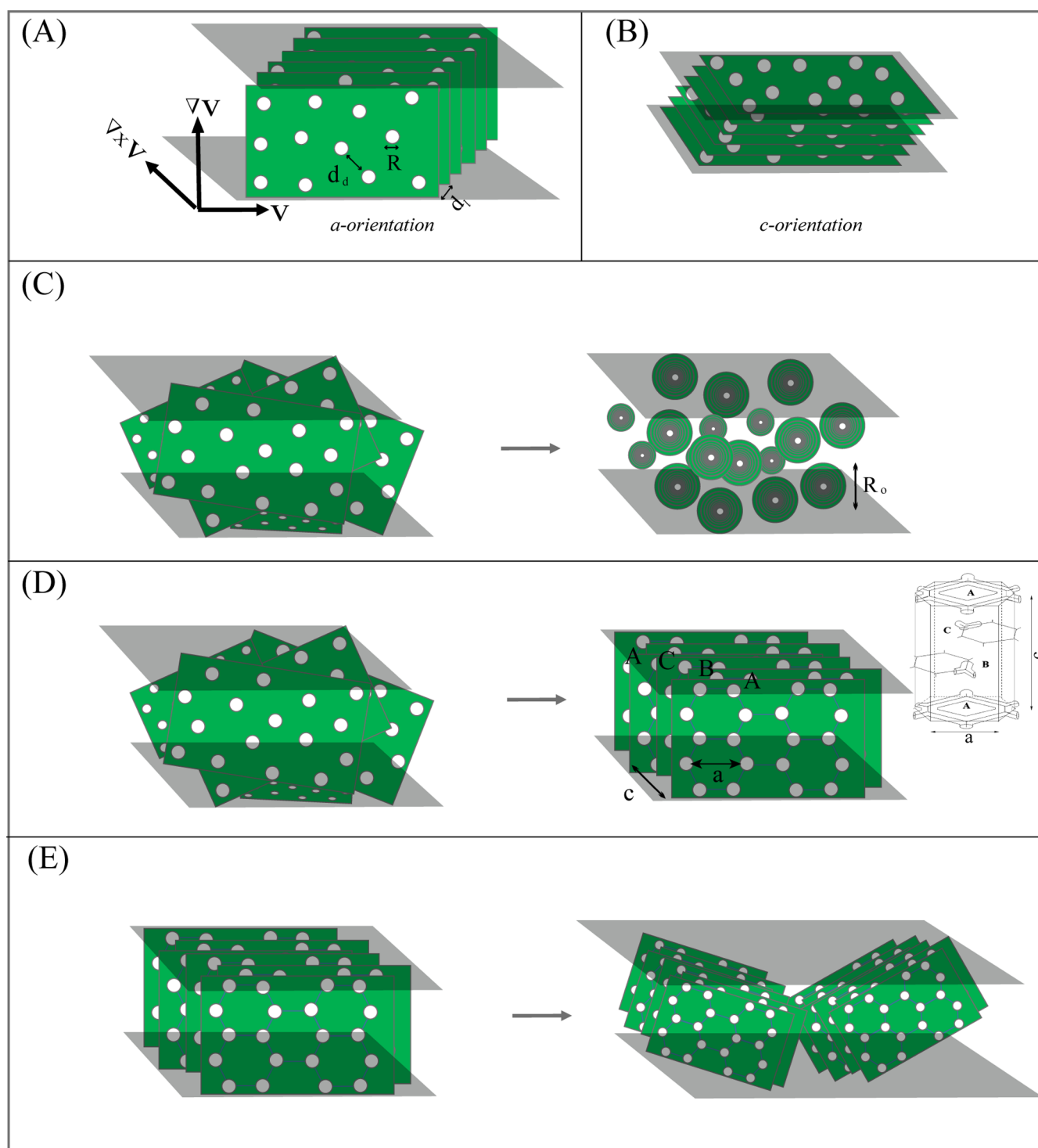
Figure 10. Schematics showing "*a*"−orientation of the random mesh phase (A), "*c*"−orientation of the random mesh phase (B), random mesh phase to onion phase transition (C), random mesh phase to ordered mesh phase transition (D), and buckling transition of the ordered mesh phase (E). A unit cell of the ordered mesh phase is shown in (D).

transform to an aligned diffraction pattern at $t \sim 70$ s (Figure 9c). The oriented (003) reflection in the vorticity direction indicates the transition to the *a*-oriented state. At $t = 75$ s, eight diffuse scattering arcs lying on (101), (012) Bragg rings are observed (Figure 9d), which is due to buckling of $R\bar{3}m$. At $t = 80$ s (Figure 9e), additional Bragg rings start appearing, indicating the onset of another structural transition. The X-ray diffraction pattern obtained at $t = 550$ s shows a stable pattern

in the steady state having a few additional reflections. Eight arcs are seen on different Bragg rings. Considering all the Bragg rings, the diffraction pattern can be indexed to two $R\bar{3}m$ phases with different lattice parameters (Supporting Information, Table S8). Due to high viscosity, the concentrated $R\bar{3}m$ phase was not studied in the Couette geometry to avoid breaking of the Couette glass geometry.

CONCLUSIONS

Using techniques such as rheo-SAXS, rheo-SALS, and microscopy, the present study has shown two striking consequences of shear flow on the random and ordered mesh phases: (i) a random mesh phase subjected to shear develops in-plane hexagonal ordering of pores and gets locked into a 3D structure to form the $R\bar{3}m$ phase; (ii) shearing of $R\bar{3}m$ results in the isomorphic twinning and buckling of bilayers out of the shear plane with the subsequent coexistence of two $R\bar{3}m$ phases with different lattice parameters. Shear is known to predominantly induce or anneal defects in colloidal crystals, although occasionally, they can order textural defects that occur in polydomain samples.[42] We argue that under shear, the NEPT from the random mesh phase to the ordered mesh phase is likely to be a more general feature of the mesh phases and is expected in surfactant−water systems where the random mesh phase and the ordered mesh phase are present adjacent to each other in the equilibrium phase diagram. A crucial point to be noted is that the equilibrium phase transition from a random mesh phase to an ordered mesh phase occurs with decreasing water content where the correlation length of the pores increases with the surfactant's weight fraction (ϕ). Intriguingly, here in our studies, the lamellar d-spacing decreases under shear only at higher values of ϕ where the NEPT appears, providing us with a clue to the origin of this NEPT. We propose that the decrease in the bilayer separation under shear increases the strength of the interaction potential which locks them into a 3D lattice due to the in-plane modulations. This decrease in the lamellar periodicity can arise possibly from the squeezing out of the water from the adjacent bilayers of crystallites or alternately due to the increase in the average size of the pores.

Further, rheology of the rhombohedral mesh phase probed in two complimentary experimental geometries (the plate−plate geometry and Couette geometry) indicate a shear alignment, followed by isomorphic twinning and buckling of the bilayers out of the shear plane. For the ordered mesh phase sheared in a Couette geometry, the buckling and twinning which is observed more toward the stator near the center of the gap could be related to the plastic deformation at high shear rates, akin to those observed in soft colloidal crystals.[43] We cannot rule out completely the other possibility that the bilayers of the ordered mesh phase under shear roll into the multilamellar cylinders arranged in a hexagonal or tetragonal array giving rise to six or eight arcs in the (101), (012) Bragg rings. In this case, large fluctuations in the viscosity even after a long time (Figures 7 and 9) can be due to the changing orientation of these cylinders under shear. However, the decrease in viscosity does not support the formation of cylinders since rolling up of lamellae into cylinders usually increases the resistance to flow and results in increased viscosity.[44] A more detailed study would be required to probe the structure and underlying mechanism of the buckling phenomena in ordered mesh phases.

In order to draw a functional relationship between the timescale of NEPT and the shear rate, one has to check whether the transition is a strain-controlled or shear rate-controlled process. If it is a strain-controlled process, one expects inverse relationship between the timescale and the shear rate.[45] Otherwise, for the shear rate/stress-controlled process, a power-law dependence of the timescale with the applied shear rate/stress is expected. However, a detailed study

is required to establish this, a future direction of our study. We hope that our experimental studies will motivate a quantitative theoretical understanding of shear-induced transitions in concentrated mixed surfactant systems.

ASSOCIATED CONTENT

ⓈⒾ Supporting Information

The Supporting Information is available free of charge at https://pubs.acs.org/doi/10.1021/acs.langmuir.0c03660.

> Estimation of a single defect's volume, shear study of L_{α}^{D} of the CPC−SHN−water system, equilibrium SAXS and SALS study of $R\bar{3}m$, and rheo-SALS during the flow curve of $R\bar{3}m$ (PDF)

AUTHOR INFORMATION

Corresponding Author

A. K. Sood − *Department of Physics, Indian Institute of Science, Bangalore 560012, India;* ⓘ orcid.org/0000-0002-4157-361X; Email: asood@iisc.ac.in

Authors

Pradip K. Bera − *Department of Physics, Indian Institute of Science, Bangalore 560012, India;* ⓘ orcid.org/0000-0003-0124-4747

Vikram Rathee − *Department of Physics, Indian Institute of Science, Bangalore 560012, India;* Present Address: Okinawa Institute of Science and Technology Graduate University, Okinawa, Japan.

Rema Krishnaswamy − *Department of Physics, Indian Institute of Science, Bangalore 560012, India;* Present Address: School of Arts and Sciences, Azim Premji University, Bangalore, 560100, India.

Complete contact information is available at:
https://pubs.acs.org/10.1021/acs.langmuir.0c03660

Author Contributions

§P.K.B. and V.R. contributed equally to this work.

Notes

The authors declare no competing financial interest.

ACKNOWLEDGMENTS

REFERENCES

(1) Kekicheff, P.; Tiddy, G. J. T. Structure of the intermediate phase and its transformation to lamellar phase in the lithium perfluorooctanoate/water system. *J. Phys. Chem.* **1989**, *93*, 2520−2526.

(2) Krishnaswamy, R.; Ghosh, S. K.; Lakshmanan, S.; Raghunathan, V. A.; Sood, A. K. Phase behavior of concentrated aqueous solutions of cetyltrimethylammonium bromide (CTAB) and sodium hydroxy naphthoate (SHN). *Langmuir* **2005**, *21*, 10439−10443.

(3) Gupta, S. P.; Raghunathan, V. A. Controlling the thermodynamic stability of intermediate phases in a cationic-amphiphile−water system with strongly binding counterions. *Phys. Rev. E: Stat., Nonlinear, Soft Matter Phys.* **2013**, *88*, 012503.

(4) Cates, M. E.; Candau, S. J. Statics and dynamics of worm-like surfactant micelles. *J. Phys.: Condens. Matter* **1990**, *2*, 6869.

(5) Holmes, M. C.; Leaver, M. S. Intermediate Phases. In *Bicontinuous Liquid Crystals*; Lynch, M. L., Spicer, P. T., Eds.; *Surfactant Science Series*; Taylor & Francis: Boca Raton, 2005; Vol. 127, pp 15−39.

(6) Funari, S. S.; Holmes, M. C.; Tiddy, G. J. T. Microscopy, X-ray diffraction, and NMR studies of lyotropic liquid crystal phases in the C22EO6/water system: a new intermediate phase. *J. Phys. Chem.* **1992**, *96*, 11029−11038.

(7) Leaver, M.; Fogden, A.; Holmes, M.; Fairhurst, C. Structural Models of theR3̄mIntermediate Mesh Phase in Nonionic Surfactant Water Mixtures. *Langmuir* **2001**, *17*, 35−46.

(8) Ghosh, S. K.; Ganapathy, R.; Krishnaswamy, R.; Bellare, J.; Raghunathan, V. A.; Sood, A. K. Structure of mesh phases in a cationic surfactant system with strongly bound counterions. *Langmuir* **2007**, *23*, 3606−3614.

(9) Lucassen-Reynders, E. H.; Lucassen, J.; Giles, D. Surface and bulk properties of mixed anionic/cationic surfactant systems in equilibrium surface tensions. *J. Colloid Interface Sci.* **1981**, *81*, 150−157.

(10) Manohar, C.; Rao, U. R. K.; Valaulikar, B. S.; Iyer, R. M. On the origin of viscoelasticity in micellar solutions of cetyltrimethyl-lammonium bromide and sodium salicylate. *J. Chem. Soc., Chem. Commun.* **1986**, 379−381.

(11) Kaler, E. W.; Herrington, K. L.; Murthy, A. K.; Zasadzinski, J. A. N. Phase behavior and structures of mixtures of anionic and cationic surfactants. *J. Phys. Chem.* **1992**, *96*, 6698−6707.

(12) Yatcilla, M. T.; Herrington, K. L.; Brasher, L. L.; Kaler, E. W.; Chiruvolu, S.; Zasadzinski, J. A. Phase behavior of aqueous mixtures of cetyltrimethylammonium bromide (CTAB) and sodium octyl sulfate (SOS). *J. Phys. Chem.* **1996**, *100*, 5874−5879.

(13) Blandamer, M. J.; Briggs, B.; Cullis, P. M.; Engberts, J. B. F. N. Titration microcalorimetry of mixed alkyltrimethylammonium bromide surfactant aqueous solutions. *Phys. Chem. Chem. Phys.* **2000**, *2*, 5146−5153.

(14) Rand, R. P.; Luzzati, V. X-ray diffraction study in water of lipids extracted from human erythrocytes: the position of cholesterol in the lipid lamellae. *Biophys. J.* **1968**, *8*, 125−137.

(15) Hyde, S. T.; Schröder, G. E. Novel surfactant mesostructural topologies: between lamellae and columnar (hexagonal) forms. *Curr. Opin. Colloid Interface Sci.* **2003**, *8*, 5−14.

(16) Yang, L.; Huang, H. W. A rhombohedral phase of lipid containing a membrane fusion intermediate structure. *Biophys. J.* **2003**, *84*, 1808−1817.

(17) Sakamoto, K.; Morishita, T.; Aburai, K.; Ito, D.; Imura, T.; Sakai, K.; Abe, M.; Nakase, I.; Futaki, S.; Sakai, H. Direct entry of Cell-Penetrating Peptide can be controlled by maneuvering the membrane curvature. *Sci. Rep.* **2021**, *11*, 31.

(18) Diat, O.; Roux, D.; Nallet, F. d. r. Effect of shear on a lyotropic lamellar phase. *J. Phys. II* **1993**, *3*, 1427−1452.

(19) Bergenholtz, J.; Wagner, N. J. Formation of AOT/brine multilamellar vesicles. *Langmuir* **1996**, *12*, 3122−3126.

(20) Zipfel, J.; Berghausen, J.; Lindner, P.; Richtering, W. Influence of shear on lyotropic lamellar phases with different membrane defects. *J. Phys. Chem. B* **1999**, *103*, 2841−2849.

(21) Koschoreck, S.; Fujii, S.; Lindner, P.; Richtering, W. Multilamellar vesicles ("onions") under shear quench: pathway of discontinuous size growth. *Rheol. Acta* **2009**, *48*, 231.

(22) Großkopf, S.; Tiersch, B.; Koetz, J.; Mix, A.; Hellweg, T. Shear-Induced Transformation of Polymer-Rich Lamellar Phases to Micron-Sized Vesicles. *Langmuir* **2019**, *35*, 3048.

(23) Zilman, A. G.; Granek, R. Undulation instability of lamellar phases under shear: A mechanism for onion formation? *Eur. Phys. J. B* **1999**, *11*, 593.

(24) Ramaswamy, S. Shear-induced collapse of the dilute lamellar phase. *Phys. Rev. Lett.* **1992**, *69*, 112.

(25) Cates, M. E.; Milner, S. T. Role of shear in the isotropic-to-lamellar transition. *Phys. Rev. Lett.* **1989**, *62*, 1856.

(26) Raghunathan, V. A. Mesh phases of surfactant-water systems. *J. Indian Inst. Sci.* **2008**, *88*, 197−210.

(27) Luzzati, V.; Mustacchi, H.; Skoulios, A.; Husson, F. La structure des colloïdes d'association. I. Les phases liquide−cristallines des systèmes amphiphile−eau. *Acta Crystallogr.* **1960**, *13*, 660−667.

(28) Kékicheff, P. From cylinders to bilayers: A structural study of phase transformations in a lyotropic liquid crystal. *Mol. Cryst. Liq. Cryst.* **1991**, *198*, 131−144.

(29) Fairhurst, C. E.; Holmes, M. C.; Leaver, M. S. Structure and morphology of the intermediate phase region in the nonionic surfactant C16EO6/water system. *Langmuir* **1997**, *13*, 4964−4975.

(30) Holmes, M. C. Intermediate phases of surfactant-water mixtures. *Curr. Opin. Colloid Interface Sci.* **1998**, *3*, 485−492.

(31) Rathee, V.; Krishnaswamy, R.; Pal, A.; Raghunathan, V. A.; Impéror-Clerc, M.; Pansu, B.; Sood, A. K. Reversible shear-induced crystallization above equilibrium freezing temperature in a lyotropic surfactant system. *Proc. Natl. Acad. Sci. U.S.A.* **2013**, *110*, 14849−14854.

(32) Mendes, E.; Menon, S. V. G. Vesicle to micelle transitions in surfactant mixtures induced by shear. *Chem. Phys. Lett.* **1997**, *275*, 477−484.

(33) Fairhurst, C. E.; Holmes, M. C.; Leaver, M. S. Shear Alignment of a Rhombohedral Mesh Phase in Aqueous Mixtures of a Long Chain Nonionic Surfactant. *Langmuir* **1996**, *12*, 6336−6340.

(34) Struth, B.; Hyun, K.; Kats, E.; Meins, T.; Walther, M.; Wilhelm, M.; Grübel, G. Observation of new states of liquid crystal 8CB under nonlinear shear conditions as observed via a novel and unique rheology/small-angle x-ray scattering combination. *Langmuir* **2011**, *27*, 2880−2887.

(35) Goulian, M.; Milner, S. T. Shear alignment and instability of smectic phases. *Phys. Rev. Lett.* **1995**, *74*, 1775.

(36) Escalante, J. I.; Gradzielski, M.; Hoffmann, H.; Mortensen, K. Shear-induced transition of originally undisturbed lamellar phase to vesicle phase. *Langmuir* **2000**, *16*, 8653−8663.

(37) Samuels, R. J. Small-angle light scattering from optically anisotropic spheres and disks. Theory and experimental verification. *J. Polym. Sci., Polym. Phys. Ed.* **1971**, *9*, 2165−2246.

(38) Wunenburger, A. S.; Colin, A.; Leng, J.; Arnéodo, A.; Roux, D. Oscillating viscosity in a lyotropic lamellar phase under shear flow. *Phys. Rev. Lett.* **2001**, *86*, 1374.

(39) Bruinsma, R.; Rabin, Y. Shear-flow enhancement and suppression of fluctuations in smectic liquid crystals. *Phys. Rev. A: At., Mol., Opt. Phys.* **1992**, *45*, 994.

(40) Silmore, K. S.; Strano, M.; Swan, J. W. Buckling, Crumpling, and Tumbling of Semiflexible Sheets in Simple Shear Flow. *Soft Matter* **2021**, *17*, 4707. Accepted Article

(41) Hamley, I. W. Structure and flow behaviour of block copolymers. *J. Phys.: Condens. Matter* **2001**, *13*, R643.

(42) Chatterjee, S.; Anna, S. L. Formation and ordering of topological defect arrays produced by dilatational strain and shear flow in smectic-Aliquid crystals. *Phys. Rev. E: Stat., Nonlinear, Soft Matter Phys.* **2012**, *85*, 011701.

(43) Taheri, S. M.; Rosenfeldt, S.; Fischer, S.; Bösecke, P.; Narayanan, T.; Lindner, P.; Förster, S. Shear-induced macroscopic "Siamese" twins in soft colloidal crystals. *Soft Matter* **2013**, *9*, 8464−8475.

(44) Zipfel, J.; Nettesheim, F.; Lindner, P.; Le, T. D.; Olsson, U.; Richtering, W. Cylindrical intermediates in a shear-induced lamellar-to-vesicle transition. *Europhys. Lett.* **2001**, *53*, 335.

(45) Fujii, S.; Yamamoto, Y. Kinetics of the orientation transition in the lyotropic lamellar phase. *J. Biorheology* **2016**, *30*, 27−33.